ACS APPLIED MATERIALS & INTERFACES

www.acsami.org

Research Article

Vapor–Liquid–Solid Growth of Site-Controlled Monolayer MoS_2 Films Via Pressure-Induc ed Supercritical Phase Nucleation

Qi-Bo Wang, Qin-Qin Xu,* Ming-Zhe Yang, Zhong-Shuai Wu, Xiao-Chuan Xia, Jian-Zhong Yin, and Zhen-Hua Han

Cite This: *ACS Appl. Mater. Interfaces* 2023, 15, 17396–17405

Read Online

ACCESS | Metrics & More | Article Recommendations | Supporting Information

ABSTRACT: In this study, a novel pressure-induced supercritical phase nucleation method is proposed to synthesize monolayer MoS_2 films, which is promoter free and can avoid contamination of films derived from these heterogeneous promoters in most of the existing techniques. The low-crystallinity and size-controlled $MoO_2(acac)_2$ particles are recrystallized on the substrate via the pressure-sensitive solvent capacity of supercritical CO_2 and these particles are used as growth sites. The size of single-crystal MoS_2 on the substrate is found to be dependent on the wetting area of the pyrolyzed precursor droplets (MoO_2) on the surface, and the formation of continuous films with high coverage is mainly controlled by the coalescence of MoO_2 droplets. It is enhanced by the increase of the nucleation site density, which can be adjusted by the supersaturation of the supercritical fluid solution. Our findings pave a new way for the controllable growth of MoS_2 and other two-dimensional materials and provide sufficient and valuable evidence for vapor–liquid–solid growth.

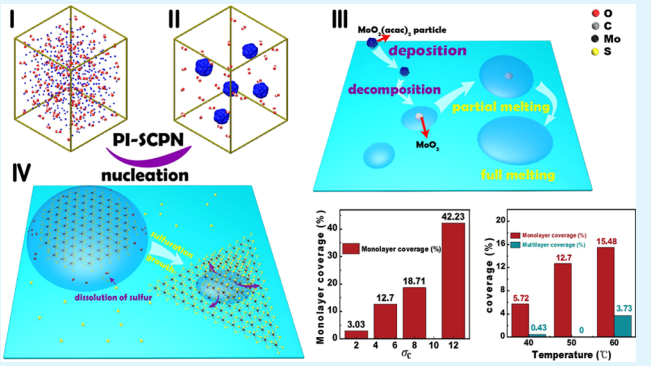

KEYWORDS: *MoS_2, vapor–liquid–solid growth, supercritical fluid, chemical vapor deposition, sulfurization, growth mechanism*

INTRODUCTION

Two-dimensional transition metal dichalcogenides (TMDCs) attract tremendous interest in electronic and optical applications[1−4] because of their layer-dependent band gaps.[5] Despite the excellent properties of TMDCs, such as abundant electronic, physical, and optical properties,[6,7] there is a limitation of nonuniformity in the growth. Therefore, controlled growth of high-quality and large-area TMDC films is crucial. Chemical vapor deposition (CVD)[8] is utilized as the most suitable method for growing two-dimensional films because of its advantages such as low cost, easy operation, and large scale.[8−11] MoS_2, as a typical TMDCs, has the most systematic study of its CVD growth mechanism.[12−15] The conventional CVD growth mechanism is a vapor–solid–solid reaction, depending on the evaporation of inorganic volatile powder precursors such as MoO_3[16,17] and MoO_2[18,19] and sulfurization in the gas phase to form MoS_2, which can deposit on arbitrary substrates.[20] However, the spatial distribution of precursor vapor concentration is inhomogeneous, resulting in monolayer MoS_2 domains with nonuniform sizes on the substrate.[13,21] Furthermore, whether the surface sulfurization reaction of precursors[22,23] or surface nucleation growth after gas phase sulfurization[24,25] is utilized, random nucleation sites are inevitably generated on the substrate or on the monolayer MoS_2, which degrades the film quality. In addition, to control the location and density of nucleation sites on the surface, Li et al.[26] utilized gold as a heterogeneous nucleation site to grow MoS_2, but the residual gold species were difficult to remove.

Subsequently, in order to overcome spatial inhomogeneities in CVD, metal–organic complexes with low volatile temperatures are introduced in metal–organic CVD (MOCVD).[27,28] Typically, the growth temperatures in MOCVD are lower to adapt growth on substrates with low melting temperatures such as plastics (PET, PEN, PI, etc),[29] which results in poor crystallinity of MoS_2, reducing carrier mobility and chemical stability, limiting its application.[30] In addition, to improve the homogeneity and continuity of monolayer MoS_2 by increasing domain size, some scholars introduce alkali metals to assist the growth.[29,31−33] With the effect of alkali metals, eutectic intermediates containing alkali metal molybdate and molybdenum oxide are formed during the growth process. The low melting point of the eutectic intermediates facilitates the reduction of nucleation and lateral growth of large monolayers of MoS_2.[32] Recently, Li et al.[34] proposed a vapor–liquid–solid (VLS) mechanism for the NaCl-assisted synthesis of MoS_2

Received: January 31, 2023
Accepted: March 16, 2023
Published: March 23, 2023

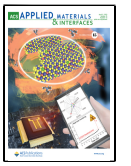

https://doi.org/10.1021/acsami.3c01407
ACS Appl. Mater. Interfaces 2023, 15, 17396–17405

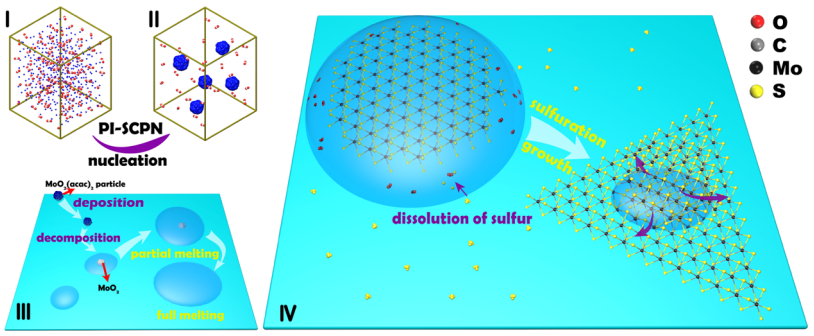

Figure 1. Schematic of VLS growth of MoS_2 with the pyrolysis and sulfurization of $MoO_2(acac)_2$ on a sapphire surface. Pressure-induced supercritical phase nucleation to deposit $MoO_2(acac)_2$ particles on Al_2O_3. (I) Dissolution of $MoO_2(acac)_2$, (II) recrystallization of $MoO_2(acac)_2$, and (III) high-temperature melting of MoO_2 from $MoO_2(acac)_2$ pyrolysis. (IV) Sulfuration of precursors to form MoS_2 films.

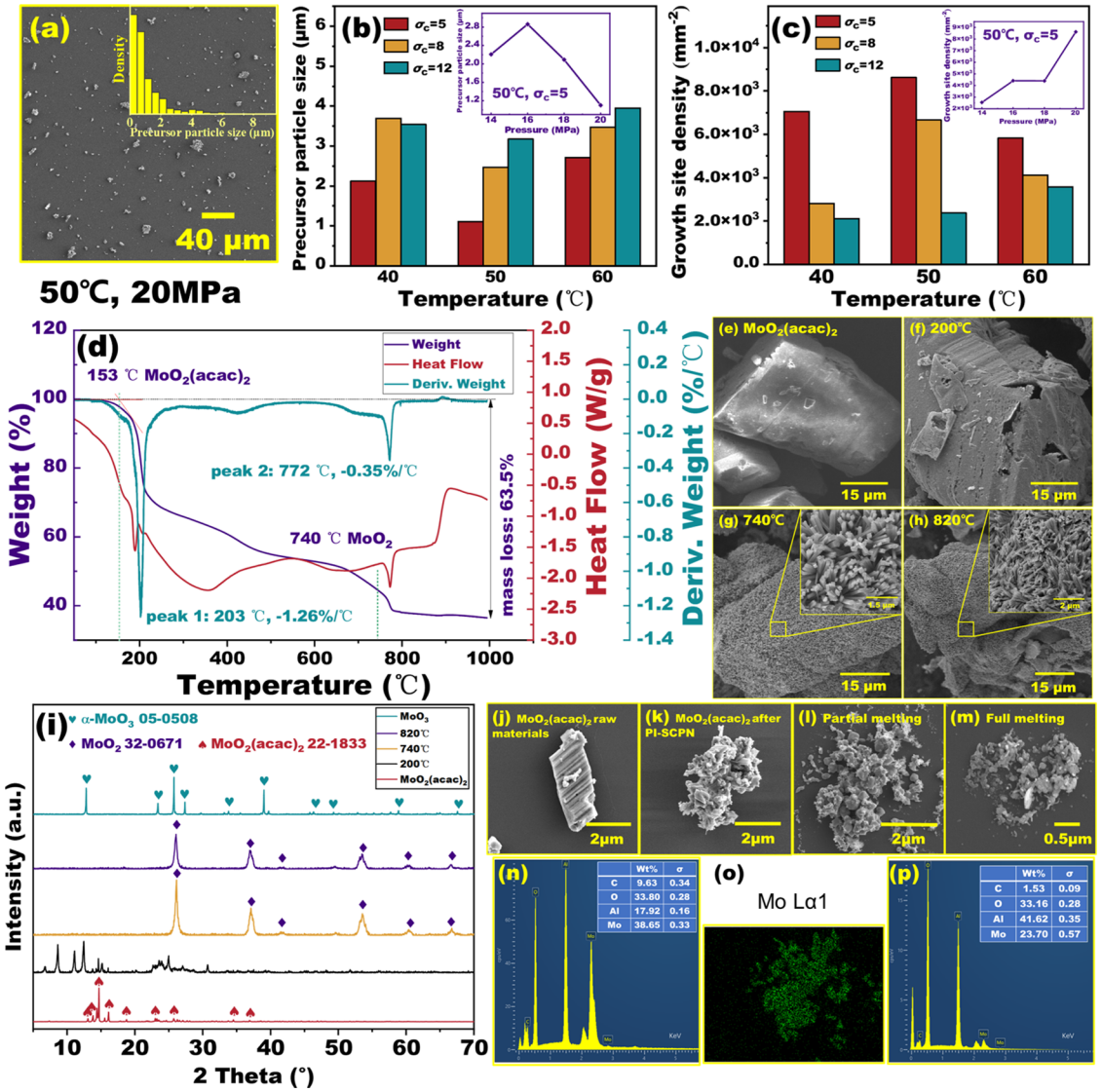

Figure 2. (a) SEM images of $MoO_2(acac)_2$ particles deposited on the sapphire at 50 °C, 20 MPa, σ_c = 5. $MoO_2(acac)_2$ particle size (b) and growth site density (c) at various temperatures, pressures, and supersaturations. (d) TG analysis of $MoO_2(acac)_2$. (e) SEM images of the $MoO_2(acac)_2$ raw material. (f–h) SEM images and (i) XRD patterns of the products obtained from the decomposition of $MoO_2(acac)_2$ at different temperatures. (j) SEM images of the internal crystal morphology of the $MoO_2(acac)_2$ raw material. SEM images of $MoO_2(acac)_2$ (k) after PI-SCPN and at annealing for (l) 1 min and (m) 10 min. (n–p) EDS analysis corresponding to k–m.

nanoribbons. They suggested that the formation of molten Na–O–Mo droplets at the growth sites mediated the growth of MoS_2 in a "crawling mode." The following year, Li et al.[35] used nonvolatile alkali molybdates and tungstates (e.g., $Na_2Mo_2O_7$, Na_2MoO_4,[36] and Na_2WO_4[37]) with low vapor pressure and suitable melting points to prepare high-quality

https://doi.org/10.1021/acsami.3c01407
ACS Appl. Mater. Interfaces 2023, 15, 17396–17405

TMDCs films by the VLS growth method. Although alkali metals do not form an alloy with MoS_2, the surface still needs to be cleaned before application, which may damage the two-dimensional structure.[38]

At present, although VLS growth is a potentially effective method for large-size and uniform TMDC film growth, the controllable synthesis and growth mechanism are still unclear. Herein, we propose a pressure-induced supercritical phase nucleation (PI-SCPN) method for the deposition of the precursor to grow MoS_2 films with controllable nucleation sites and coverage. $MoO_2(acac)_2$ is used as a precursor because of its moderate solubility in supercritical carbon dioxide ($scCO_2$). Benefiting from the pressure-sensitive solvent capacity of $scCO_2$, the recrystallized $MoO_2(acac)_2$ particle is composed of several small crystals and has low crystallinity. At the optimum growth temperature of MoS_2 (820 °C), $MoO_2(acac)_2$ is fully pyrolyzed into MoO_2 droplets, followed by being sulfurized into MoS_2. The precursor particles replace the promoter as the growth site, the density of the growth site is tuned by thermodynamic parameters, and the monolayer coverage is tuned by supersaturation. The wetting area of the droplets determines the domain size at 10^1 μm. When the supersaturation exceeds 12, large continuous films are formed, which is caused by the coalescence of MoO_2 droplets. Finally, the quality and homogeneity of MoS_2 grown by this method are evaluated by electron microscopy, spectroscopy, and electrical measurements.

RESULTS AND DISCUSSION

The strategy for controllable synthesis of MoS_2 films via CVD growth is schematically illustrated in Figure 1. In order to deposit precursor particles on a sapphire substrate, a recrystallization method, PI-SCPN, was performed. This equipment is illustrated in Figure S1. During the PI-SCPN process, supercritical carbon dioxide ($scCO_2$), a solvent, had the solvent capacity to dissolve most of the metal−organic complexes, such as substances containing ligands of acetylacetonate (acac), carbonyl (CO), or 2,2,6,6-tetramethyl-3,5-heptanedionato (thd) when the temperature and pressure were above its critical point ($T_c \approx 31.4$ °C, $p_c \approx 7.4$ MPa).[39] After full dissolution, the thermodynamic state was changed leading to the precipitation and deposition of the solute ($MoO_2(acac)_2$) on the target substrate, as shown in Figure 1(I−III). The substrate with deposited Mo precursors was placed horizontally on quartz boats to grow MoS_2. The whole growth process consists of two stages. The thermal decomposition reaction of the precursor particles at the surface produced MoO_2 particles, as shown in Figure 1(III). Subsequently, MoO_2 formed molten droplets at 820 °C and reacted with gaseous S powder to form MoS_2 micron sheets inside the droplets. The detailed results and the mechanistic analysis are described in Figure 1(IV). More details about the above-mentioned synthesis are shown in the Experimental Section.

Nucleation and Growth of Precursor Seeds by PI-SCPN. In our previous study, the formation of $MoO_2(acac)_2$ critical nuclei was systematically investigated in relation to the nonideality of $scCO_2$ and supersaturation.[40] Therefore, we will focus on the growth behavior of critical nuclei and the deposition process in the following. The SEM images of $MoO_2(acac)_2$ particles deposited on the sapphire at an initial temperature, pressure, and supersaturation of 50 °C, 20 MPa, and $\sigma_c = 5$, respectively, are shown in Figure 2a, with a statistical average particle size (d_p) of ∼1.1 μm. The size of the particles and the nucleation rate (I) were related to the thermodynamic state of the solvent. Furthermore, the size of precursor particles was controlled by nucleation and growth processes.[41] In the nucleation stage, higher pressure, temperature, and supersaturation were beneficial for nucleus formation.[40] However, after the formation of the critical nucleus, the growth process was critical to the final particle size. The nucleus continuously "absorbed" solute molecules and became larger or collided with other nuclei, leading to dissipation or agglomeration. In addition, some agglomerated structures with larger sizes of about 6−8 μm were found in the figure, which was caused by the agglomeration formed by the inevitable collision of particles during the CO_2 expansion. This collision was related to the nucleation rate but also to the pressure relief rate and the device structure. Therefore, the process of growth in the supercritical phase was extremely complex.

In order to balance the effect of the growth process on the d_p as much as possible, the same pressure relief rate of 3.71 MPa/s was used in our experiments to investigate the d_p and I at various conditions, as shown in Figure 2b,c. The d_p was found to be larger at high supersaturation at $p = 20$ MPa, and there was a trend of increasing with temperature. The inset of Figure 2b shows the particle size obtained at $T = 50$ °C, $\sigma_c = 5$. It was found that d_p decreased with increasing pressure at pressures between 16 and 20 MPa. In addition, the nucleation rate increased with increasing pressure, which indicated that the nuclei were more involved in the nucleation process in this pressure region, resulting in less solute involved in the growth, and finally smaller size particles were formed. Moreover, at the high nucleation rate, the nuclei have a higher probability of collision with each other, and this collision also led to the increase of the particle size, like the larger particles in Figure 2a. In contrast, we found that the size of the particles was smaller at a pressure of 14 MPa, which was due to the fact that at lower nucleation rates, the probability of collision between particles was smaller, and therefore the particles formed were mostly grown by single nuclei. The corresponding SEM images are shown in Figure S3.

In thin film growth, arbitrary discontinuities on a smooth surface could serve as nucleation sites for MoS_2 formation. Therefore, the deposition of dispersed precursor particles or agglomerated structures on the substrate by PI-SCPN could act as growth sites. Hence, the number of particles per unit area was defined as growth site density (growth site density, GSD), as shown in Figure 2c. At the same temperature, as the supersaturation increased, collisions between particles during nucleation led to agglomeration, causing a decrease in GSD. In addition, we found that GSD was significantly different at the same temperature and different supersaturation, with the highest GSD at 50 °C. This was because GSD was jointly determined by the nucleation rate and interparticle collisions during growth. At lower temperatures (40 °C), the nucleation rate with low collision probability was smaller, resulting in a smaller GSD. As the temperature increased (50 °C), the nucleation rate increased, resulting in the increase of GSD. When the temperature was increased further (60 °C), the increase in collision probability resulted in a decrease in GSD. The density at 20 MPa increased by 260% compared to 14 MPa, which indicated that increasing the initial pressure can effectively increase GSD, as shown in the inset of Figure 2c. The effect of GSD on MoS_2 film coverage and domain size will

https://doi.org/10.1021/acsami.3c01407
ACS Appl. Mater. Interfaces 2023, 15, 17396−17405

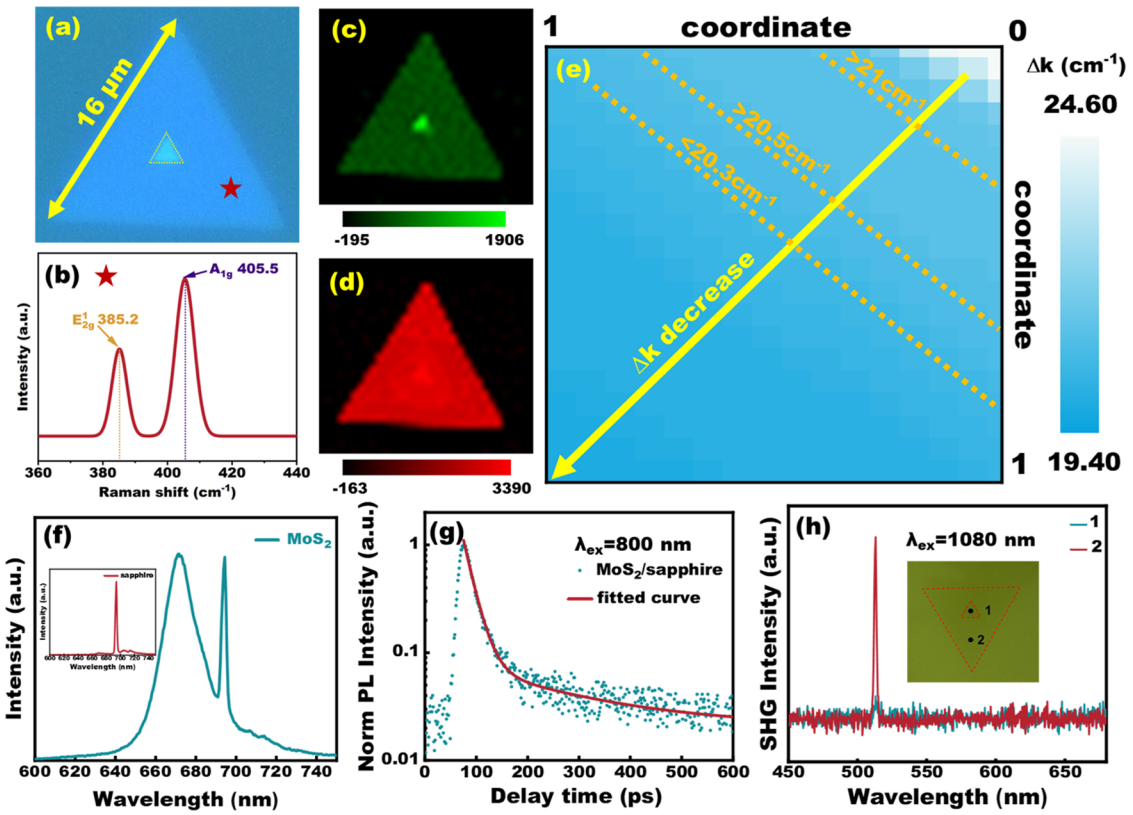

Figure 3. Spectroscopic analyses of MoS_2. (a) OM image of the MoS_2 domain. (b) Corresponding Raman spectra of MoS_2 at the marked point in (a). (c, d) Corresponding Raman mapping on the intensity of E_{2g}^1 and A_{1g} modes, respectively. (e) Heat map of MoS_2-specific frequency difference. (f) PL and (g) TRPL at the marked point in (a), respectively. (h) SHG of 2H phase MoS_2.

be described in the subsequent section Sulfurization of the Precursors.

Thermal Decomposition of the Precursor. Thermogravimetry (TG) and derivative thermogravimetry (DTG) analyses of $MoO_2(acac)_2$ are shown in Figure 2d. The TG analysis in the temperature range from 50 to 1000 °C was measured by using a heating rate of 5 °C/min at a flow rate of 50 sccm argon gas. The total weight loss ratio of $MoO_2(acac)_2$ was 63.5% in temperatures ranging from 50 to 1000 °C, and the weight loss process can be divided into six stages, as shown in Table S2. There was a strong weight loss peak for $MoO_2(acac)_2$ at 203 °C, peak 1. Also, there was a strong heat absorption peak near this temperature. It indicated that $MoO_2(acac)_2$ underwent a thermal decomposition process rather than a sublimation process at 203 °C, which was consistent with the results reported by Mannei et al.[38] Moreover, a comparison of SEM images of the raw material in Figure 2e,f and the the product at 200 °C revealed that the formation of pores and cracks on the surface was due to heating. As shown in Figure 2i, the characteristic peaks of XRD changed significantly at 200 °C compared with the peaks of $MoO_2(acac)_2$, which proved that the cause of the weight loss was thermal decomposition.

The product obtained from the decomposition of pure $MoO_2(acac)_2$ in an argon atmosphere was MoO_2 with a theoretical weight loss ratio of 60.12%.[38] However, $MoO_2(acac)_2$ was a viscous powder at room temperature and contained 1 wt % acetylacetone, a stabilizer, which volatilizes at 140 °C. Therefore, the theoretical weight loss ratio for complete decomposition was reduced to 59.52% at 774 °C. Furthermore, it was found that only the characteristic peak of crystalline monoclinic MoO_2 (#JCPDS32-0671, $P21$, lattice parameter of a = 5.61 Å, b = 4.68 Å, c = 5.54 Å, β = 119.37°) was present in the XRD of the product at 740 °C, as shown in Figure 2i, and the weight loss was 52.03% < 59.52%. With the SEM image of the product at 740 °C, it can be concluded that most of the $MoO_2(acac)_2$ had decomposed into "french fries" MoO_2 at the surface, while the internal $MoO_2(acac)_2$ had not been fully decomposed, as shown in Figure 2g. As the temperature was 772 °C, a large weight loss peak 2 was found and a heat absorption peak existed at 774 °C, which indicated that the internal $MoO_2(acac)_2$ was decomposed. Subsequently, the SEM image of the product at 820 °C showed that the surface "french fries" of MoO_2 changed to "wheat ears" and the XRD results showed that it was still MoO_2. Therefore, it was inferred that MoO_2 was in a molten state at 820 °C, and MoO_2 evaporated slowly in the temperature range of 774−820 °C. Furthermore, no MoO_3 characteristic peaks were found by measuring the XRD of the products at different temperatures.

In order to illustrate the melting state of the precursor particles on the sapphire after PI-SCPN, annealing experiments at different times were carried out at 820 °C and in an argon atmosphere. The particle size after PI-SCPN was smaller (Figure 2k) than that of the $MoO_2(acac)_2$ raw material (Figure 2j), and most of the particles were agglomerated by a number of tiny clusters, and this agglomeration structure was beneficial to the heat exchange. After 1 min of annealing, the particles were partially melted and fine acicular structures were present near the particles, as shown in Figure 2l. Figure 2o shows the EDS mapping images of Mo. As the annealing time was increased to 10 min (as shown in Figure 2m), the particles

https://doi.org/10.1021/acsami.3c01407
ACS Appl. Mater. Interfaces 2023, 15, 17396−17405

Table 1. Fitting Parameters of the PL Decay Curve Using Biexponential Mode Convolution of Gaussian Response Functions

sample	growth mechanism	τ_1 (ps)	A_1 (%)	τ_2 (ps)	A_2 (%)	τ (ps)
MoS_2/Al_2O_3 (this work)	VLS	19.28	94.98	211.35	5.02	28.92
MoS_2/quartz[44]	VSS	84	74	1650	26	
MoS_2/SiO_2−7 μm[44]	VSS	51	95	980	5	

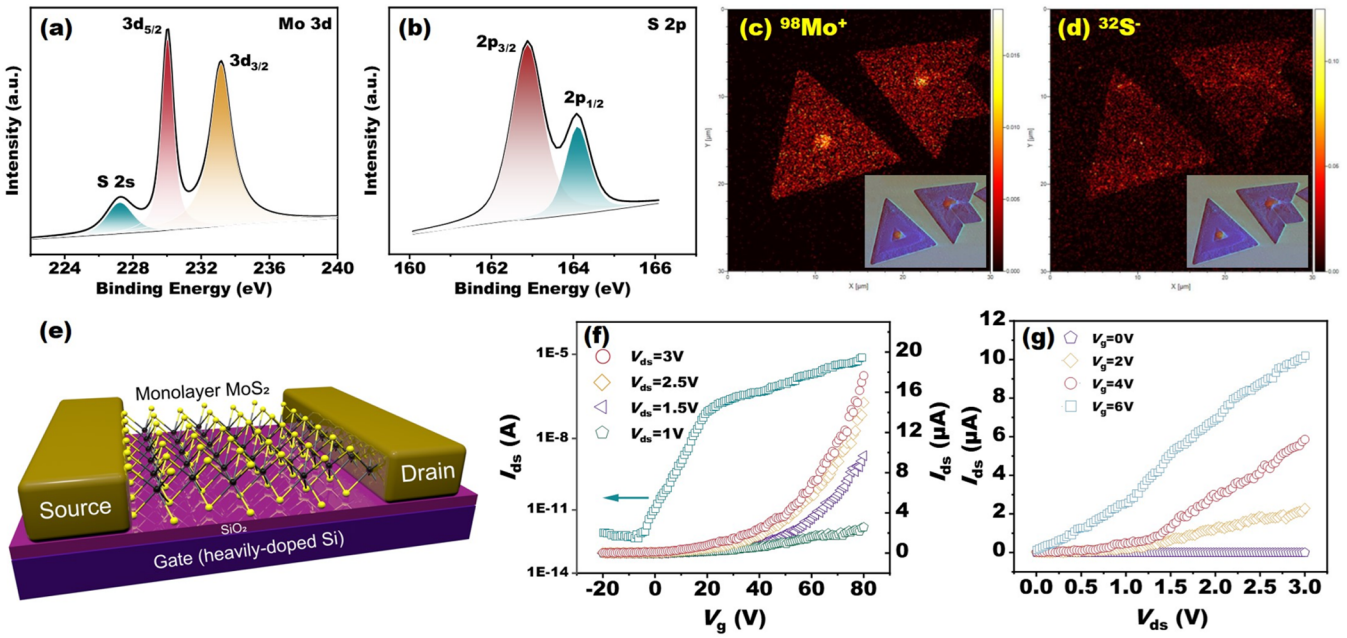

Figure 4. Quality characterization of MoS_2 and performance of the field effect transistor. (a, b) XPS spectra of monolayer MoS_2 on the sapphire substrate showing the fine spectra of Mo 3d and S 2p, respectively. (c, d) ToF-SIMS mapping of $^{98}Mo^+$ and $^{32}S^-$ in MoS_2, respectively. (e) Schematic illustration of a back-gate monolayer MoS_2 FETs. (f) Typical transport property of MoS_2 FETs. (g) Corresponding output performance of the MoS_2 FETs.

were fully melted, and the EDS analysis showed that C was reduced to 1.53 wt %, as shown in Figure 2p. This was also a direct indication that the particles reached the molten state at 820 °C and that the particle size decreased and melted completely with increasing annealing time. In addition, as indirect evidence, it was found that a MoS_2 nanoribbon was grown near the upstream substrate edge by sulfurization of the precursors at 820 °C, which was similar to that reported in the literature,[42] as shown in Figure S4. One of the reasons for the generation of the MoS_2 nanoribbon was the orientation movement of the molten precursors on the surface.

Sulfurization of the Precursors. Through the investigation of the effect of sulfurization parameters on the growth of MoS_2, we determined the optimum growth conditions as follows: a growth temperature of 820 °C, a carrier gas flow rate of 40 sccm, and a growth time of 20 min. Detailed parameter effects can be found in Section 9 (Supporting Information). Moreover, the precursors used in the sulfurization were processed through PI-SCPN at T = 50 °C, σ_c = 5, and p = 20 MPa. To evaluate the crystal quality of MoS_2, a series of spectroscopic analyses were first performed, as shown in Figure 3. The domain size of MoS_2 was about 16 μm. Figure 3b shows typical Raman modes of a MoS_2 flake at 385.2 cm^{-1} (E_{2g}^1) and 405.5 cm^{-1} (A_{1g}), which was performed at the marked point, as shown in Figure 3a. The full-width at half-maximum (FWHM) values of E_{2g}^1 (6.6 cm^{-1}) and A_{1g} (7.1 cm^{-1}) indicated higher crystallinity of monolayer MoS_2.[43] The specific frequency difference Δk ($\Delta k = A_{1g} - E_{2g}^1$) was 20.3 cm^{-1}, highly illustrative of the monolayer nature of the obtained flake, which was slightly lower than that reported in the literature for monolayer molybdenum disulfide (20.5 cm^{-1}).[8] In addition, Raman mapping on the intensity of the E_{2g}^1 mode shown in Figure 3c was lower than the intensity of the A_{1g} mode shown in Figure 3d and manifested a uniform color contrast at the monolayer, further demonstrating the uniformity of thickness and good crystallinity.

Subsequently, the Δk at different positions of this flake was statistically calculated. With the center of the flake as the coordinate origin, the value of the peak spacing at the center is shown in the upper right corner of Figure 3e, reaching a maximum of 24.6 cm^{-1}, which was close to the specific frequency difference of bulk MoS_2. Moreover, the Δk of the multilayer MoS_2 at the center was decreased with increasing distance from the origin, which indicated that the number of MoS_2 layers was gradually decreasing. This phenomenon was caused by the inability of the molten MoO_2 at the center to diffuse sufficiently to grow into a uniform film, resulting in a higher thickness growing in the center of the droplet than the edge thickness, while in the monolayer region, the peak spacing was more between 19.8 and 20.3 cm^{-1} and decreased slightly as it was far from the central region. In addition, the typical PL spectrum shows a sharp excitonic A peak at 1.85 eV (670 nm) with a narrow full-width at half-maximum. Furthermore, with a relatively low intensity (similar to that of the sapphire), it confirmed that our VLS-derived monolayer MoS_2 had a high crystallinity.

To investigate the exciton dynamics of VLS-grown monolayer MoS_2, TRPL measurements were conducted on

https://doi.org/10.1021/acsami.3c01407
ACS Appl. Mater. Interfaces 2023, 15, 17396−17405

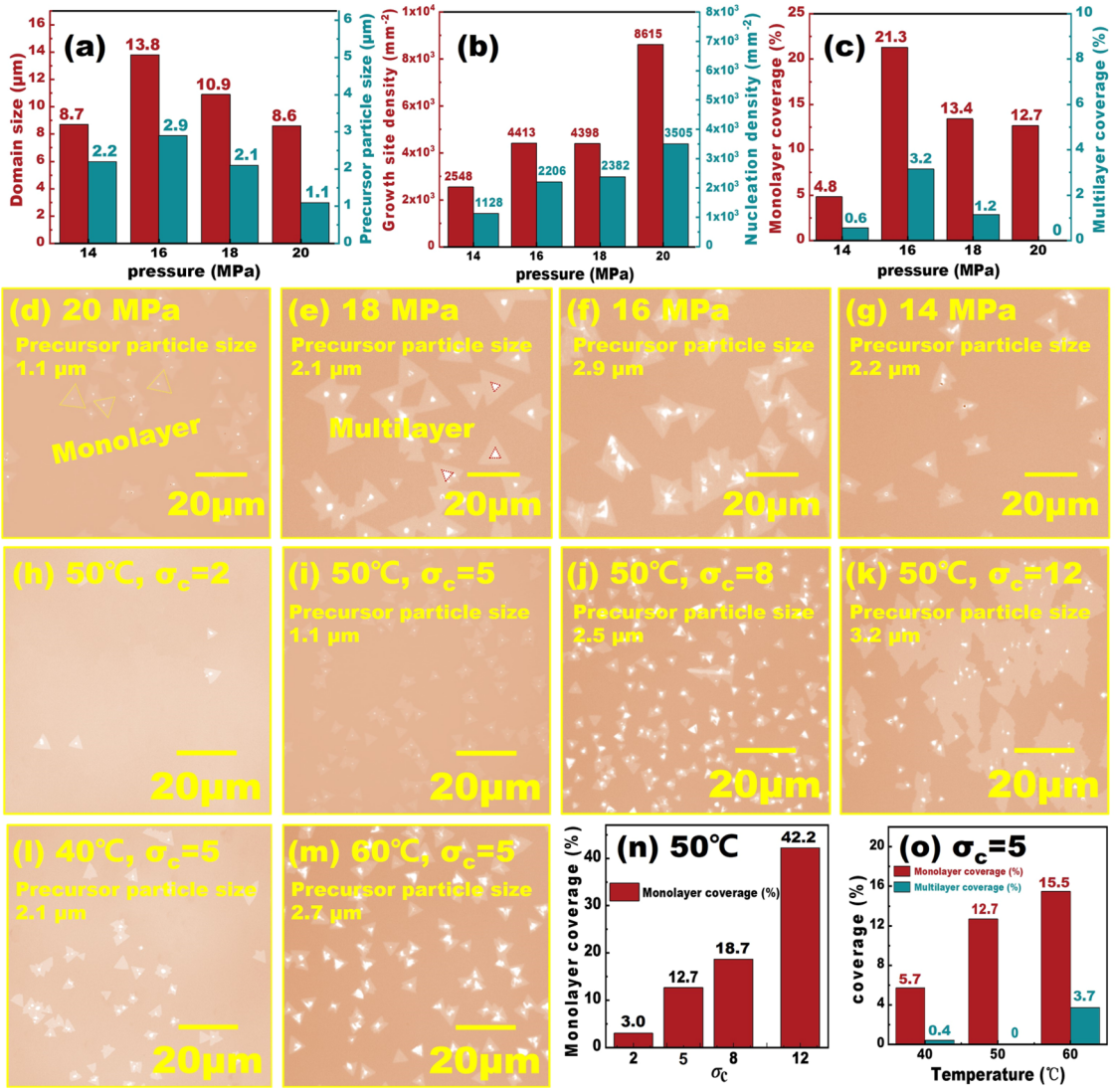

Figure 5. (a) Variation of the MoS_2 domain size with the precursor particle size at different pressures. (b) Relationship between precursor growth site density and nucleation density. (c) MoS_2 monolayer and multilayer coverage. (d–g) OM images of MoS_2 grown at different pressures. (h–m) OM images of MoS_2 grown at different dissolution temperatures and supersaturation. (n) Effect of supersaturation on monolayer coverage. (o) Effect of the dissolution temperature on monolayer and multilayer coverage.

the as-prepared MoS_2/Al_2O_3. As shown in Figure 3g, the PL decay curve (red) of monolayer MoS_2 on sapphire at an excitation of 800 nm was fitting by utilizing a biexponential decay process

$$I(t) = A_1 \exp(-t/\tau_1) + A_2 \exp(-t/\tau_2)$$

where the time constants τ_1 and τ_2 are fast decay lifetimes and long lifetimes, respectively, and A_1 (A_2) represents fast (slow) components. The fitting parameters for PL decay curves are listed in Table 1. The fast decay lifetime τ_1 was 19.82 ps and the long lifetime τ_2 was 211.35 ps, which were shorter than VSS-grown MoS_2.[44] In semiconductors, the short lifetime τ_1 was related to carrier-phonon scattering and the long lifetime τ_2 was attributed to the direct interband electron–hole complexation process.[44] Hence, the strong confinement of the excitons within the atomically thin layer resulted in a large contribution weight of a carrier-phonon scattering decay channel to exciton recombination of up to 94.98% in MoS_2/Al_2O_3.[45] This contribution was identical to the system of MoS_2/SiO_2 (Table 1), which indicated that both carrier–phonon scattering and interband leap processes were regulated by the Purcell effect.[46,47]

Second harmonic generation (SHG), as a second-order nonlinear optical phenomenon, could be used to characterize the structural symmetry of 2D materials.[42,48] The SHG characterization of the bilayer MoS_2 is shown in Figure 3h, with an incident wavelength of 1080 nm. At the bilayer position 1, it exhibited an SHG peak with lower intensity, while at the monolayer position 2, a single SHG peak located at 513 nm was observed. This indicated that our VLS-grown MoS_2 was a 2H phase.[49]

Subsequently, in order to assess the quality of MoS_2 synthesized by our method, the chemical state and composition of the MoS_2 film were analyzed by X-ray photoelectron spectroscopy (XPS, Figure 4a,b). All of the spectra had charge correction for the C 1s adventitious carbon peak at 284.8 eV to compensate for the sample charge. In Mo 3d spectra, the peaks of Mo^{4+} $3d_{5/2}$ and Mo^{4+} $3d_{3/2}$ were located at 230.1 and 233.2 eV, respectively. In S 2p spectra, S^{2-} $2p_{3/2}$ and S^{2-} $2p_{1/2}$ were located at 162.9 and 164.1 eV,

https://doi.org/10.1021/acsami.3c01407
ACS Appl. Mater. Interfaces 2023, 15, 17396–17405

respectively. The above-mentioned results were similar to the binding energy of Mo and S in monolayer MoS_2 grown by the VLS method using Na_2MoO_4[35] and the VSS method using MoO.[50] By integrating the area of Mo and S signals, the ratio of Mo and S was about 1:2, which confirmed the expectation of high-quality MoS_2.[51] Moreover, time-of-flight secondary ion mass spectrometry (ToF-SIMS) was used to characterize the distribution of $^{98}Mo^+$ and $^{32}S^-$ in MoS_2 (Figure 4c,d). ToF-SIMS provided rich information about materials within a depth of <10 nm from the surface and had high-sensitivity chemical mapping characteristics, which was conducive to analyzing TMDC films.[52] Negative ion mode analysis and positive ion mode analysis were used for S and Mo, respectively. Due to the thin monolayer MoS_2, the signal of one mode was weak (in this paper, the signal of S was weak). In the mapping image, the uniformly distributed Mo and S ions showed that the film was highly homogeneous. However, there was multilayer MoS_2 at the center of the crystal domain, resulting in a strong signal.

The electrical properties of monolayer MoS_2 grown by our method were examined by measuring the transfer property and output performance of MoS_2 field-effect transistors (FETs). Monolayer MoS_2 grown on sapphire was transferred to a SiO_2/Si substrate (SiO_2 thickness was 285 nm). Figure 4e shows the FET structure with a back-gate structure and the material of the source and drain was Au. The electron mobility μ_{FE} was calculated by the following equation:

$$\mu_{FE} = \frac{L}{W \cdot C_{OX} \cdot V_{ds}} \cdot \frac{dI_{ds}}{dV_g}$$

where L = 0.58 μm, W = 10 μm, C_{OX} = 1.15 × 10^{-8} F·cm^{-2}, V_{ds}, and dI_{ds}/dV_g are the channel length, channel width, gate capacitance, applied drain−source bias, and transconductance, respectively. From the analysis of typical transport properties (Figure 4f), the mobility and on/off ratio of our MoS_2 FETs were 14.6 cm^2 V^{-1} s^{-1} and ∼10^7, respectively, which were comparable to MoS_2 grown by Na_2MoO_4.[35] Figure 4g shows the I_{ds}−V_{ds} measurement on FETs with gate voltage from 0 to 6 V. The nonlinear curve suggested that there was Schottky contact between MoS_2 and the Au electrode.

Growth Mechanism of MoS_2. The growth of the crystal began at the crystal−environment phase interface, where the environmental phase could be vapor, liquid, or melting phase. In the VLS growth of TMDCs, MoS_2 was first formed on the surface wetted with the substrate inside the precursor droplet, which was related to the surface energy between different phases. In our method, although the growth mechanism was similar to the gas−liquid−solid growth mechanism reported in the literature, the precursor was gradually depleted with the sulfurization reaction. Therefore, the state of precursor particles on the surface could have a significant impact on the properties of MoS_2, such as domain size and coverage, and the detailed analysis was as follows:

In Figure 5a, the domain size of MoS_2 was estimated from the precursor particle size. The dissolution pressure can significantly affect the precursor particle size. When the pressure ranged from 14 to 20 MPa, the precursor particle size ranged from 1.1 to 2.9 μm and the domain size was 8.6−13.8 μm. In addition, an interesting finding was that there was an ∼2-fold relationship between the GSD and the nucleation density (ND), and ND increased with GSD, as shown in Figure 5b. This suggested that the smaller precursor particles might have volatilized during the growth process and some of the MoS_2 might have merged. Although the domain size tended to increase with increasing particle size, the domain size was about 10^1 μm order of magnitude and no significant increase in the domain size was found, as shown in Figure 5d−g. Moreover, the domain size was determined by the diffusion process of the molten precursors on the surface. At a certain temperature and with the same hydrophilicity, there was a limit to the maximum area (i.e., the wetting area) that the melted particles diffused on the surface. With the effect of surface tension, appropriately increasing the particle size cannot increase the wetting area. However, this might lead to large particles with more precursors, and after a portion of the precursors had grown to form a monolayer of MoS_2 with the largest size, the remaining precursors could only continue to grow above the monolayer to form a multilayer MoS_2, as shown in the highlighted regions in Figure 5e,f. According to the crystal growth kinetics, the advancement rate of the step decreases with the increase of the step height. Therefore, it was known from our experiments that the lateral dimensions of the multilayer were smaller than those of the monolayer, and larger-size particles might not form large-size MoS_2. After lateral epitaxy to a critical size, MoS_2 tended to grow longitudinally to form multilayer structures.

Furthermore, in Figure 5e,g, it was found that the domain size of MoS_2 obtained at almost the same precursor particle size was significantly different, with larger domains obtained at 18 MPa, which was speculated to be related to the PI-SCPN stage. In previous studies, the crystallinity of precursor particles was gradually decreased with increasing pressure, and the agglomerated structure consisted of smaller-size clusters at high pressure, which resulted in more complete melting in the sulfurization stage. In Figure 5c, the percentages of multilayers to monolayers at 18 and 14 MPa were 0.09 and 0.11, respectively, which indicated that dissolution pressure had a nonsignificant effect on longitudinal growth.

Subsequently, the film coverage was substantially increased without changing the growth parameters only by increasing the precursor supersaturation. The coverage of monolayer MoS_2 increased with the increase of supersaturation, i.e., the coverage increased from 3.03 to 42.23% at supersaturation between 2 and 12 at 50 °C, as shown in Figure 5h−k. It was found that the monolayer coverage increased with increasing dissolution temperature, but the multilayer coverage seemed not to have a direct relationship with the dissolution temperature, as shown in Figure 5o. In addition, it was found that the domain size obtained at different temperatures was approximately the same, differing only in the percentage of multilayers. However, large-area monolayer films were obtained at σ_c = 12, 50 °C, which was due to droplet coalescence caused by higher supersaturation. As previously stated, there was a limit to the wetting area of molten MoO_2, and the limit wetting area $A_{d_o,max}$ was related to the particle size, where d_0 was the maximum precursor particle size to reach $A_{d_o,max}$, i.e., as the precursor particle size $d \le d_o$, the wetting area $A \le A_{d_o,max}$. Within $A_{d_o,max}$, the precursor reacted with the sulfur dissolved within the droplet to form a monolayer MoS_2, while the excess precursor then only continued to grow on the already grown monolayer MoS_2 to form a multilayer structure. In combination with the experimental results, it can be seen that d_o was between 2.9 and 3.2 μm in this method. When $d > d_o$, the melt wetting area was increased, which could increase the domain size of MoS_2. When the density of molten droplets was large, the probability

https://doi.org/10.1021/acsami.3c01407
ACS Appl. Mater. Interfaces 2023, 15, 17396−17405

of two-drop fusion was increased, resulting in the formation of films with a larger domain size or higher coverage, as shown in Figure 5k. In addition, this critical particle size also existed when other precursors were used and the films were prepared by using the gas−liquid−solid growth and limiting the lateral dimensions of the films.

CONCLUSIONS

In summary, we proposed and demonstrated the PI-SCPN method regulating precursor deposition to grow monolayer MoS_2 films by using $MoO_2(acac)_2$ as a precursor. The nucleation site and coverage of MoS_2 could be tuned by controlling the state of precursor particles on the surface through dissolution parameters and supersaturation. Each precursor particle replaced the promoter as the growth site, avoiding the possible contamination of films. When the supersaturation σ_c = 12, a continuous film with coverage greater than 40% was formed. The quality and uniformity of MoS_2 at the optimum growth conditions were carefully evaluated by a series of optical and electrical characterizations. Attributed to the solubility of $scCO_2$ in most metal−organic complexes, the recrystallization of precursors was expected to be an effective method for the deposition of other precursors to grow films. Moreover, utilizing more complex sulfurization precursors (such as H_2S or organic sulfur), continuous homoepitaxial growth, and optimizing the transfer process during sulfurization were expected to improve the uniformity and monolayer coverage of the film and layer number control.

EXPERIMENTAL SECTION

Pressure-Induced Supercritical Phase Nucleation. Precursor seeds were prepared as follows: dissolution of a precursor in $scCO_2$ and pressure-induced nucleation. $MoO_2(acac)_2$ was first dissolved in $scCO_2$, and the pressure and temperature in the dissolving autoclave were adjusted to a predetermined value, which was maintained for 24 h to ensure that the precursor was fully dissolved. The valve opening between the dissolving autoclave and the deposition tank was then precisely adjusted to ensure that the pressure was relieved at a uniform rate of 3.71 MPa/s. The precursor solute was crystallized in the direction of the reduced pressure and deposited on the sapphire substrate in the deposition tank to form seeds. $MoO_2(acac)_2$ solubility data, substrate cleaning treatment, and other details are available in the Supporting Information.

Growth of MoS_2. MoS_2 films were grown by the sulfurization of precursor seeds in an atmospheric-pressure tube furnace. At the optimal growth conditions, 1 g of S powder was placed in the upstream region, and the heating temperature of the S zone was 270 °C. The sapphire substrate was placed horizontally in the downstream region with a heating temperature of 820 °C. The MoS_2 films were completely formed at 820 °C within a reaction time of 20 min. Argon gas was used as a carrier gas with 40 sccm. The sapphire substrate was grown under an argon atmosphere at 40 sccm for 20 min. After the furnace cooled to room temperature, the sapphire substrate was removed.

Characterization of the Precursor and MoS_2 Films. SEM (HITACHI, SU5000, with an X-ray energy spectrometer), TG (METTLER TOLEDO, TGA/DSC3$^+$), XRD (BRUKER, D8 Advance), Raman/PL (Renishaw, inVia Qontor), TRPL/SHG (WITec, alpha-300), XPS (Thermo Fisher Scientific, K-Alpha+), and ToF-SIMS (TESCAN Amber with a ToF-SIMS detector) were used to characterize the optical and structural properties of the MoS_2 films.

ASSOCIATED CONTENT

Supporting Information

The Supporting Information is available free of charge at https://pubs.acs.org/doi/10.1021/acsami.3c01407.

Detailed PI-SCPN process and equipment, solubility data of $MoO_2(acac)_2$, effect of pressure on precursor particles and additional thermogravimetry analysis of $MoO_2(acac)_2$, parameter setting of the sulfurization process, and OM images of MoS_2 obtained at different sulfurization conditions (PDF)

AUTHOR INFORMATION

Corresponding Author

Qin-Qin Xu − *State Key Laboratory of Fine Chemicals, School of Chemical Engineering, Dalian University of Technology, 116024 Dalian, China;* orcid.org/0000-0001-9672-2259; Email: qinqinxu@dlut.edu.cn

Authors

Qi-Bo Wang − *State Key Laboratory of Fine Chemicals, School of Chemical Engineering, Dalian University of Technology, 116024 Dalian, China*

Ming-Zhe Yang − *State Key Laboratory of Fine Chemicals, School of Chemical Engineering, Dalian University of Technology, 116024 Dalian, China*

Zhong-Shuai Wu − *State Key Laboratory of Catalysis, Dalian Institute of Chemical Physics, Chinese Academy of Sciences, 116024 Dalian, China;* orcid.org/0000-0003-1851-4803

Xiao-Chuan Xia − *School of Physics & School of Microelectronics, Dalian University of Technology, 116024 Dalian, China*

Jian-Zhong Yin − *State Key Laboratory of Fine Chemicals, School of Chemical Engineering, Dalian University of Technology, 116024 Dalian, China;* orcid.org/0000-0003-4529-3743

Zhen-Hua Han − *State Key Laboratory of Fine Chemicals, School of Chemical Engineering, Dalian University of Technology, 116024 Dalian, China*

Complete contact information is available at: https://pubs.acs.org/10.1021/acsami.3c01407

Author Contributions

Q.-Q.X. conceived the idea of the PI-SCPN method and designed the device. Q.-B.W. wrote the manuscript with inputs from all authors and completed the sulfurization experiment and all of the characterization. M.-Z.Y. and Z.-H.H. performed the PI-SCPN experiments. Z.-S.W. and X.-C.X. analyzed the VLS growth mechanism. J.-Z.Y. supervised the research.

Notes

The authors declare no competing financial interest.

ACKNOWLEDGMENTS

The authors thank the Shanghai Demo Lab for the ToF-SIMS analysis. This material is based upon work supported by the National Natural Science Foundation of China (21978043) and the National Key R&D Program of China (2020YFA0710202).

REFERENCES

(1) Radisavljevic, B.; Radenovic, A.; Brivio, J.; Giacometti, V.; Kis, A. Single-layer MoS_2 transistors. *Nat. Nanotechnol.* **2011**, *6*, 147−150.

(2) Radisavljevic, B.; Kis, A. Mobility engineering and a metal–insulator transition in monolayer MoS_2. *Nat. Mater.* **2013**, *12*, 815–820.
(3) Wu, F.; Tian, H.; Shen, Y.; Hou, Z.; Ren, J.; Gou, G.; Sun, Y.; Yang, Y.; Ren, T. Vertical MoS_2 transistors with sub-1-nm gate lengths. *Nature* **2022**, *603*, 259–264.
(4) Meng, W.; Xu, F.; Yu, Z.; Tao, T.; Shao, L.; Liu, L.; Li, T.; Wen, K.; Wang, J.; He, L.; et al. Three-dimensional monolithic micro-LED display driven by atomically thin transistor matrix. *Nat. Nanotechnol.* **2021**, *16*, 1231–1236.
(5) Tongay, S.; Zhou, J.; Ataca, C.; Lo, K.; Matthews, T. S.; Li, J.; Grossman, J. C.; Wu, J. Thermally driven crossover from indirect toward direct bandgap in 2D semiconductors: $MoSe_2$ versus MoS_2. *Nano Lett.* **2012**, *12*, 5576–5580.
(6) Wang, Q. H.; Kalantar-Zadeh, K.; Kis, A.; Coleman, J. N.; Strano, M. S. Electronics and optoelectronics of two-dimensional transition metal dichalcogenides. *Nat. Nanotechnol.* **2012**, *7*, 699–712.
(7) Cai, Z.; Liu, B.; Zou, X.; Cheng, H. Chemical Vapor Deposition Growth and Applications of Two-Dimensional Materials and Their Heterostructures. *Chem. Rev.* **2018**, *118*, 6091–6133.
(8) Yang, P.; Zou, X.; Zhang, Z.; Hong, M.; Shi, J.; Chen, S.; Shu, J.; Zhao, L.; Jiang, S.; Zhou, X.; et al. Batch production of 6-inch uniform monolayer molybdenum disulfide catalyzed by sodium in glass. *Nat. Commun.* **2018**, *9*, No. 979.
(9) Elías, A. L.; Perea-López, N.; Castro-Beltrán, A.; Berkdemir, A.; Lv, R.; Feng, S.; Long, A. D.; Hayashi, T.; Kim, Y. A.; Endo, M.; et al. Controlled Synthesis and Transfer of Large-Area WS_2 Sheets: From Single Layer to Few Layers. *ACS Nano* **2013**, *7*, 5235–5242.
(10) Ji, Q.; Zhang, Y.; Zhang, Y.; Liu, Z. Chemical vapour deposition of group-VIB metal dichalcogenide monolayers: engineered substrates from amorphous to single crystalline. *Chem. Soc. Rev.* **2015**, *44*, 2587–2602.
(11) Rajan, A. G.; Warner, J. H.; Blankschtein, D.; Strano, M. S. Generalized Mechanistic Model for the Chemical Vapor Deposition of 2D Transition Metal Dichalcogenide Monolayers. *ACS Nano* **2016**, *10*, 4330–4344.
(12) Jeon, J.; Jang, S. K.; Jeon, S. M.; Yoo, G.; Jang, Y. H.; Park, J. H.; Lee, S. Layer-controlled CVD growth of large-area two-dimensional MoS_2 films. *Nanoscale* **2015**, *7*, 1688–1695.
(13) Wang, S.; Rong, Y.; Fan, Y.; Pacios, M.; Bhaskaran, H.; He, K.; Warner, J. H. Shape Evolution of Monolayer MoS_2 Crystals Grown by Chemical Vapor Deposition. *Chem. Mater.* **2014**, *26*, 6371–6379.
(14) Chen, S.; Gao, J.; Srinivasan, B. M.; Zhang, G.; Yang, M.; Chai, J.; Wang, S.; Chi, D.; Zhang, Y. Revealing the Grain Boundary Formation Mechanism and Kinetics during Polycrystalline MoS_2 Growth. *ACS Appl. Mater. Interfaces* **2019**, *11*, 46090–46100.
(15) Seravalli, L.; Bosi, M. A Review on Chemical Vapour Deposition of Two-Dimensional MoS_2 Flakes. *Materials* **2021**, *14*, 7590.
(16) Yu, H.; Liao, M.; Zhao, W.; Liu, G.; Zhou, X. J.; Wei, Z.; Xu, X.; Liu, K.; Hu, Z.; Deng, K.; et al. Wafer-Scale Growth and Transfer of Highly-Oriented Monolayer MoS_2 Continuous Films. *ACS Nano* **2017**, *11*, 12001–12007.
(17) Singh, A.; Moun, M.; Singh, R. Effect of different precursors on CVD growth of molybdenum disulfide. *J. Alloys Compd.* **2019**, *782*, 772–779.
(18) Xu, X.; Wang, Z.; Lopatin, S.; Quevedo-Lopez, M. A.; Alshareef, H. N. Wafer scale quasi single crystalline MoS_2 realized by epitaxial phase conversion. *2D Mater.* **2019**, *6*, No. 015030.
(19) Chiawchan, T.; Ramamoorthy, H.; Buapan, K.; Somphonsane, R. CVD Synthesis of Intermediate State-Free, Large-Area and Continuous MoS2 via Single-Step Vapor-Phase Sulfurization of MoO2 Precursor. *Nanomaterials* **2021**, *11*, 2642.
(20) Liu, Y.; Gu, F. A wafer-scale synthesis of monolayer MoS_2 and their field-effect transistors toward practical applications. *Nanoscale Adv.* **2021**, *3*, 2117–2138.
(21) Xu, J.; Ho, D. Modulation of the Reaction Mechanism via S/Mo: A Rational Strategy for Large-Area MoS_2 Growth. *Chem. Mater.* **2021**, *33*, 3249–3257.
(22) Cheng, Z.; Xia, M.; Hu, R.; Liang, C.; Liang, G.; Zhang, S. Single crystal monolayer MoS_2 triangles with wafer-scale spatial uniformity by MoO_3 pre-deposited chemical vapor deposition. *J. Cryst. Growth* **2017**, *480*, 6–12.
(23) Kang, S. K.; Lee, H. S. Study on Growth Parameters for Monolayer MoS_2 Synthesized by CVD Using Solution-based Metal Precursors. *Appl. Sci. Convergence Technol.* **2019**, *28*, 159–163.
(24) Hyun, C.-M.; Choi, J.; Lee, S. W.; Park, J. H.; Lee, K.; Ahn, J. Synthesis mechanism of MoS_2 layered crystals by chemical vapor deposition using MoO_3 and sulfur powders. *J. Alloys Compd.* **2018**, *765*, 380–384.
(25) Bilgin, I.; Liu, F.; Vargas, A.; Winchester, A.; Man, M. K. L.; Upmanyu, M.; Dani, K. M.; Gupta, G.; Talapatra, S.; Mohite, A. D.; Kar, S. Chemical Vapor Deposition Synthesized Atomically Thin Molybdenum Disulfide with Optoelectronic-Grade Crystalline Quality. *ACS Nano* **2015**, *9*, 8822–8832.
(26) Li, Y.; Hao, S.; DiStefano, J. G.; Murthy, A. A.; Hanson, E. D.; Xu, Y.; Wolverton, C.; Chen, X.; Dravid, V. P. Site-Specific Positioning and Patterning of MoS_2 Monolayers: The Role of Au Seeding. *ACS Nano* **2018**, *12*, 8970–8976.
(27) Mun, J.; Park, H.; Park, J.; Joung, D.; Lee, S.; Leem, J.; Myoung, J.; Park, J.; Jeong, S.; Chegal, W.; et al. High-Mobility MoS_2 Directly Grown on Polymer Substrate with Kinetics-Controlled Metal–Organic Chemical Vapor Deposition. *ACS Appl. Electron. Mater.* **2019**, *1*, 608–616.
(28) Hwangbo, S.; Hu, L.; Hoang, A. T.; Choi, J. Y.; Ahn, J. Wafer-scale monolithic integration of full-colour micro-LED display using MoS_2 transistor. *Nat. Nanotechnol.* **2022**, *17*, 500–506.
(29) Wang, Z.; Xie, Y.; Wang, H.; Wu, R.; Nan, T.; Zhan, Y.; Sun, J.; Jiang, T.; Zhao, Y.; Lei, Y.; et al. NaCl-assisted one-step growth of MoS_2-WS_2 in-plane heterostructures. *Nanotechnology* **2017**, *28*, No. 325602.
(30) Mun, J.; Kim, Y.; Kang, I.; Lim, S. K.; Lee, S. J.; Kim, J. W.; Park, H. M.; Kim, T.; Kang, S. Low-temperature growth of layered molybdenum disulphide with controlled clusters. *Sci. Rep.* **2016**, *6*, No. 21854.
(31) Kim, H.; Ovchinnikov, D.; Deiana, D.; Unuchek, D.; Kis, A. Suppressing Nucleation in Metal–Organic Chemic$_a$l Vapor Deposition of MoS2 Monolayers by Alkali Metal Halides. *Nano Lett.* **2017**, *17*, 5056–5063.
(32) Wang, P.; Lei, J.; Qu, J.; Cao, S.; Jiang, H.; He, M.; Shi, H.; Sun, X.; Gao, B.; Liu, W. Mechanism of Alkali Metal Compound-Promoted Growth of Monolayer MoS_2: Eutectic Intermediates. *Chem. Mater.* **2019**, *31*, 873–880.
(33) Chang, M.-C.; Ho, P.; Tseng, M.; Lin, F.; Hou, C.; Lin, I.; Wang, H.; Huang, P.; Chiang, C.; Yang, Y.; et al. Fast growth of large-grain and continuous MoS_2 films through a self-capping vapor-liquid-solid method. *Nat. Commun.* **2020**, *11*, No. 3682.
(34) Li, S.; Lin, Y.; Zhao, W.; Wu, J.; Wang, Z.; Hu, Z.; Shen, Y.; Tang, D.; Wang, J.; Zhang, Q.; et al. Vapour–liquid–solid growth of monolayer MoS_2 nanoribbons. *Nat. Mater.* **2018**, *17*, 535–542.
(35) Li, S.; Lin, Y.; Liu, X.; Hu, Z.; Wu, J.; Nakajima, H.; Liu, S.; Okazaki, T.; Chen, W.; Minari, T.; et al. Wafer-scale and deterministic patterned growth of monolayer MoS_2 via vapor–liquid–solid method. *Nanoscale* **2019**, *11*, 16122–16129.
(36) Yu, C.; Chang, P.; Guan, L.; Tao, J. Inward growth of monolayer MoS_2 single crystals from molten Na_2MoO_4 droplets. *Mater. Chem. Phys.* **2020**, *240*, No. 122203.
(37) Chen, C.; Yang, Y.; Zhou, X.; Xu, W.; Cui, Q.; Lu, J.; Jing, H.; Tian, D.; Xu, C.; Zhai, T.; Xu, H. Synthesis of Large-Area Uniform MoS_2–WS_2 Lateral Heterojunction Nanosheets for Photodetectors. *ACS Appl. Nano Mater.* **2021**, *4*, 5522–5530.
(38) Mannei, E.; Ayari, F.; Asedegbega-Nieto, E.; Mhamdi, M.; Guerrero-Ruiz, A. R.; Delahay, G.; Ghorbel, A. Solid–state ion exchange of molybdenum (VI) acetylacetonate into ZSM-5 zeolite. *Thermochim. Acta* **2017**, *652*, 150–159.
(39) Teoh, W. H.; Mammucari, R.; Foster, N. R. Solubility of organometallic complexes in supercritical carbon dioxide: A review. *J. Organomet. Chem.* **2013**, *724*, 102–116.

(40) Wang, Q.-B.; Xu, Q.; Yin, J.; Zhu, H.; Liu, B.; Yang, M. Development of a novel theory of pressure-induced nucleation in supercritical carbon dioxide. *CrystEngComm* **2022**, *24*, 3035−3048.
(41) Türk, M. Influence of thermodynamic behaviour and solute properties on homogeneous nucleation in supercritical solutions. *J. Supercrit. Fluids* **2000**, *18*, 169−184.
(42) Cheng, J.; Jiang, T.; Ji, Q.; Zhang, Y.; Li, Z.; Shan, Y.; Zhang, Y.; Gong, X.; Liu, W.; Wu, S. Kinetic Nature of Grain Boundary Formation in As-Grown MoS_2 Monolayers. *Adv. Mater.* **2015**, *27*, 4069−4074.
(43) Yang, Y.; Pu, H.; Li, L.; Di, J.; Lin, T.; Hu, J.; Zang, Y.; Zhang, S. Effect of Processing Parameters on Monolayer MoS2 Prepared by APCVD in a Quasiclosed Crucible. *J. Electron. Mater.* **2019**, *48*, 4947−4958.
(44) Mi, Y.; Zhang, Z.; Zhao, L.; Zhang, S.; Chen, J.; Ji, Q.; Shi, J.; Zhou, X.; Wang, R.; Shi, J.; et al. Tuning Excitonic Properties of Monolayer MoS_2 with Microsphere Cavity by High-Throughput Chemical Vapor Deposition Method. *Small* **2017**, *13*, No. 1701694.
(45) Shi, H.; Yan, R.; Bertolazzi, S.; Brivio, J.; Gao, B.; Kis, A.; Jena, D.; Xing, H. G.; Huang, L. Exciton Dynamics in Suspended Monolayer and Few-Layer MoS_2 2D Crystals. *ACS Nano* **2013**, *7*, 1072−1080.
(46) Altug, H.; Englund, D.; Vu Kovi, J. Ultrafast photonic crystal nanocavity laser. *Nat. Phys.* **2006**, *2*, 484−488.
(47) Canet-Ferrer, J.; Prieto, I.; Muñoz-Matutano, G.; Martínez, L. J.; Muñoz-Camuniez, L. E.; Llorens, J. M.; Fuster, D.; Alén, B.; González, Y.; González, L.; et al. Excitation power dependence of the Purcell effect in photonic crystal microcavity lasers with quantum wires. *Appl. Phys. Lett.* **2013**, *102*, No. 201105.
(48) Yin, X.; Ye, Z.; Chenet, D. A.; Ye, Y.; O'Brien, K.; Hone, J. C.; Zhang, X. Edge nonlinear optics on a $MoS_(2)$ atomic monolayer. *Science* **2014**, *344*, 488−490.
(49) Zeng, Z.; Sun, X.; Zhang, D.; Zheng, W.; Fan, X.; He, M.; Xu, T.; Sun, L.; Wang, X.; Pan, A. Controlled Vapor Growth and Nonlinear Optical Applications of Large-Area 3R Phase WS_2 and WSe_2 Atomic Layers. *Adv. Funct. Mater.* **2019**, *29*, No. 1806874.
(50) Yang, P.; Zhang, Z.; Sun, M.; Lin, F.; Cheng, T.; Shi, J.; Xie, C.; Shi, Y.; Jiang, S.; Huan, Y.; et al. Thickness Tunable Wedding-Cake-like MoS_2 Flakes for High-Performance Optoelectronics. *ACS Nano* **2019**, *13*, 3649−3658.
(51) Kim, I. S.; Sangwan, V. K.; Jariwala, D.; Wood, J. D.; Park, S.; Chen, K.; Shi, F.; Ruiz-Zepeda, F.; Ponce, A.; Jose-Yacaman, M.; et al. Influence of Stoichiometry on the Optical and Electrical Properties of Chemical Vapor Deposition Derived MoS_2. *ACS Nano* **2014**, *8*, 10551−10558.
(52) Chen, B.-J.; Yin, Y.; Ling, Y. ToF-SIMS study of chemical composition and formation of all-nanoparticle multilayer films. *Appl. Surf. Sci.* **2008**, *255*, 981−983.

https://doi.org/10.1021/acsami.3c01407
ACS Appl. Mater. Interfaces 2023, 15, 17396−17405